Navier-Stokes Simulations of Transonic Flows over a Wing-Fuselage Combination

Kozo Fujii*
National Aerospace Laboratory, Tokyo, Japan
and
Shigeru Obayashi†
University of Tokyo, Tokyo, Japan

Computations of transonic flows over a practical wing-fuselage geometry designed for a transonic transport aircraft are carried out using three-dimensional Reynolds-averaged "thin-layer" Navier-Stokes equations. The thin-layer approximation is extended to two directions to evaluate viscous layers on both the wing and fuselage surfaces. The LU-ADI factorization algorithm is used with the implementation of new smoothing terms. Computations are done for several angles of attack with the specified Mach and Reynolds numbers corresponding to the experiment, and the comparison of the computed surface pressure to the experimental data shows good agreement. The computed results reveal the effect of the fuselage near the wing root, especially at relatively high angles of attack. It is shown that the flow pattern when a fuselage exists is quite different from that for an isolated wing. This indicates the importance of the computation over a wing-fuselage combination using Navier-Stokes equations. The computations, which uses about 700,000 grid points, requires about 5–6 h of computer time on a Japanese supercomputer for each case.

Introduction

TO make realistic and cost-effective predictions of transport aircraft aerodynamics, reliable and efficient three-dimensional transonic flow analysis methods are required. Presently, these predictions are mainly based on solutions of transonic potential equations, and the use of these solutions actually helped the design of recently developed transport aircrafts such as Boeing 757, 767, Airbus 310 and so on.[1]

Flowfield simulations using three-dimensional Navier-Stokes codes have been in the research stage. However, with the present progress of supercomputers and numerical techniques, they are moving into a mature stage for realistic problems. The use of potential codes as design tools may be replaced by the use of "Reynolds-averaged" Navier-Stokes codes in the near future.

The use of a supercomputer is an unavoidable factor in realistic Navier-Stokes simulations. Thus, an algorithm used for that purpose should have good vectorization capability in addition to efficiency and robustness. Efforts have been made to develop such algorithms, and a number of results using supercomputers have been reported recently.[2-4] The present authors have also been engaged in developing efficient and robust three-dimensional Navier-Stokes codes. The LU-ADI algorithm used in these codes was originally developed by Obayashi and Kuwahara[5] for the two-dimensional problem. Its extension to three dimensions and application to relatively simple geometries were reported in Ref. 6. Its stability and efficiency were then improved, and the application of the improved code to a transonic flow over an isolated wing was presented in Ref. 7 (also see Ref. 8).

In the present paper, viscous transonic flows over a realistic transport wing-fuselage combination are simulated using the three-dimensional Reynolds-averaged Navier-Stokes equations. The LU-ADI algorithm, shown to be suitable for such simulations requiring a large amount of grid points and computer time, is used. The "thin-layer" approximation in two directions is adopted to evaluate the viscous layers on both the wing and fuselage. A new type of nonlinear smoothing term developed in Ref. 9 is implemented.

The body geometry is a wing-fuselage combination called "W-18" which was designed for transonic transport aircraft. Computations are carried out for several angles of attack with specified Mach and Reynolds numbers corresponding to an experimental study of the same geometry. Each computation requires several hours of computer time on a Japanese supercomputer. The computed result demonstrates an interesting separated flow pattern near the wing-fuselage junction for relatively high-angle of attack cases, which indicates an important effect of the fuselage's existence. The comparison of the *Cp* distribution with the experiment on both the fuselage and the wing shows good agreement, and the results in general indicate that the application of the present Navier-Stokes code to complete aircraft geometries is quite promising.

Governing Equations and Numerical Algorithm

Compressible Navier-Stokes Equations

The partial differential equations in the generalized coordinate system governing the three-dimensional flow of an unsteady, ideal gas can be written in conservation-law form:

$$\partial_\tau \hat{Q} + \partial_\xi \hat{E} + \partial_\eta \hat{F} + \partial_\zeta \hat{G} = Re^{-1}\left(\partial_\eta \hat{S}_1 + \partial_\zeta \hat{S}_2\right) \quad (1)$$

where $\hat{Q}$, $\hat{F}$, $\hat{G}$, $\hat{H}$, $\hat{S}_1$, and $\hat{S}_2$ are

$$\hat{Q} = J^{-1}\begin{bmatrix} \rho \\ \rho u \\ \rho v \\ \rho w \\ e \end{bmatrix}, \qquad \hat{E} = J^{-1}\begin{bmatrix} \rho U \\ \rho u U + \xi_x p \\ \rho v U + \xi_y p \\ \rho w U + \xi_z p \\ U(e+p) - \xi_t p \end{bmatrix}$$

Presented as Paper 86-1831 at the AIAA Applied Aerodynamics Conference, San Diego, CA, June 9–11, 1986; received June 9, 1986; revision received April 15, 1987.

*Senior Research Scientist. Member AIAA.
†Graduate Student, Department of Aeronautics. Student Member AIAA.

$$\hat{F} = J^{-1}\begin{bmatrix} \rho V \\ \rho uV + \eta_x p \\ \rho uV + \eta_y p \\ \rho wV + \eta_z p \\ V(e+p) - \eta_t p \end{bmatrix}, \qquad \hat{G} = J^{-1}\begin{bmatrix} \rho W \\ \rho uW + \zeta_x p \\ \rho vW + \zeta_y p \\ \rho wW + \zeta_z p \\ W(e+p) - \zeta_t p \end{bmatrix}$$

with

$$\hat{S}_1 = J^{-1}\begin{bmatrix} 0 \\ \mu m_1 u_\eta + (\mu/3) m_2 \eta_x \\ \mu m_1 v_\eta + (\mu/3) m_2 \eta_y \\ \mu m_1 w_\eta + (\mu/3) m_2 \eta_z \\ \mu m_1 m_3 + (\mu/3) m_2 (\eta_x u + \eta_y v + \eta_z w) \end{bmatrix}$$

$$\hat{S}_2 = J^{-1}\begin{bmatrix} 0 \\ \mu n_1 u_\zeta + (\mu/3) n_2 \zeta_x \\ \mu n_1 v_\zeta + (\mu/3) n_2 \zeta_y \\ \mu n_1 w_\zeta + (\mu/3) n_2 \zeta_z \\ \mu n_1 n_3 + (\mu/3) n_2 (\zeta_x u + \zeta_y v + \zeta_z w) \end{bmatrix}$$

Here

$$m_1 = \eta_x^2 + \eta_y^2 + \eta_z^2, \qquad m_2 = \eta_x u_\eta + \eta_y v_\eta + \eta_z w_\eta,$$

$$m_3 = (u^2 + v^2 + w^2)_\eta/2 + \kappa Pr^{-1}(\gamma - 1)^{-1}(a^2)_\eta;$$

$$n_1 = \zeta_x^2 + \zeta_y^2 + \zeta_z^2, \qquad n_2 = \zeta_x u_\zeta + \zeta_y v_\zeta + \zeta_z w_\zeta,$$

$$n_3 = (u^2 + v^2 + w^2)_\zeta/2 + \kappa Pr^{-1}(\gamma - 1)^{-1}(a^2)_\zeta$$

and; U, V, and W are unscaled contravariant velocities.

For high-Reynolds-number flows, the viscous effects are confined to a thin layer near the wall boundary and are dominated by the viscous terms associated with the strain rates normal to the wall. The terms associated with the strain rates along the body surface are comparatively small and negligible. Also, since the computational grid is highly concentrated near the body surface, resulting in the mesh aspect ratio becoming very large, the inclusion of these terms would not change the solution. Thus, the thin-layer approximation has been introduced in Eqs. (1), as is typically done in most Navier-Stokes computations. In Eqs. (1), however, the concept of thin-layer approximation is extended to two directions, since viscous layers on both the fuselage and the wing should be considered. The cross-derivative terms are neglected, and only the $\hat{S}_{1\eta}$ and $\hat{S}_{2\zeta}$ terms are retained.

The pressure, density, and velocity components are related to the energy for an ideal gas by the following equations:

$$p = (\gamma - 1)\left[e - \rho(u^2 + v^2 + w^2)/2\right] \tag{2}$$

In the following computations, the viscosity coefficient in Eqs. (1) is computed as the sum of $\mu + \mu_t$. The turbulent eddy viscosity μ_t is computed by using a two-layer algebraic viscosity model, due to Baldwin and Lomax, with a modified distance. The length scales are difficult to define near the junction of a fuselage and a wing. In the present study, the evaluation of length scales proposed by Hung for his bluntfin study[10] are adopted. The metrics are evaluated using second-order central-difference formulas for interior points and three-point, one-sided formulas at the boundaries. The steady-state solution of Eqs. (1) is obtained by time integration in a time-asymptotic fashion.

LU-ADI Factorization Algorithm

The numerical algorithm used here is the new LU-ADI factorization method proposed by the present authors.[7] Implicit time integration methods with a delta form are widely used for solving steady-state problems, since the steady-state solutions are indifferent to the left-hand side operators. The most commonly used is the approximate factorization method proposed by Beam and Warming used in Ref. 11. The present LU-ADI factorization method belongs to a category of schemes that reduces the work of inverting the left-hand side operators of the Beam and Warming method. Each ADI operator is decomposed into the product of lower and upper bidiagonal matrices by using a flux vector splitting technique and a diagonally dominant factorization. It should be noted that the right-hand side remains to be the same as the Beam-Warming method where central differencing is used.

The Beam-Warming factorization applied to Eqs. (1) is written as

$$\begin{aligned} &\left(I + h\delta_\xi \hat{A}^n - D_i|_\xi\right)\left(I + h\delta_\eta \hat{B}^n - D_i|_\eta\right) \\ &\quad \times \left(I + h\delta_\zeta \hat{C}^n - hRe^{-1}\bar{\delta}_\zeta J^{-1}\hat{M}^n J - D_i|_\zeta\right)\Delta\hat{Q}^n \\ &\quad = -h\left[\delta_\xi \hat{E}^n + \delta_\eta \hat{F}^n + \delta_\zeta \hat{G}^n - Re^{-1}\bar{\delta}_\zeta \hat{S}^n\right] \\ &\quad -\left(D_e|_\xi + D_e|_\eta + D_e|_\zeta\right)\hat{Q}^n \end{aligned} \tag{3}$$

where h is the time step and δ is a central finite-difference operator. The implicit and explicit artificial dissipation terms D_i and D_e should be added to the left-hand and right-hand sides, respectively, to maintain stability. The basic algorithm is first-order in time and second-order in space. For the convective terms on the right-hand side, fourth-order differencing is used, except near the boundaries. Maintenance of

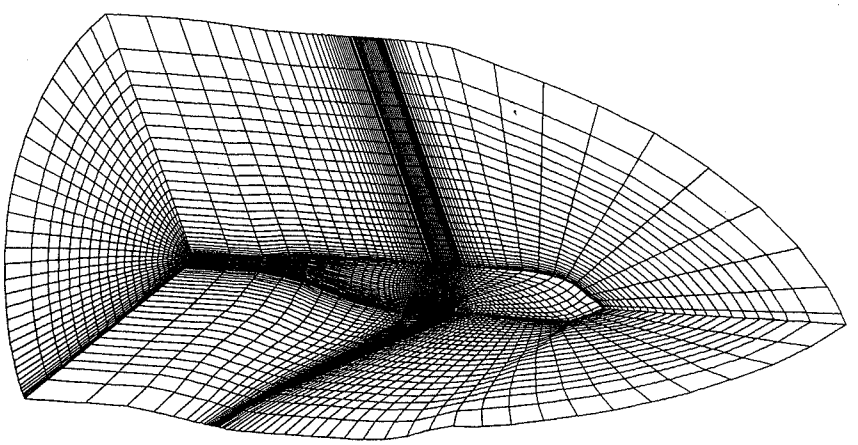

Fig. 1 Overall view of the discretized region of the grids (upper half of the computational domain).

the freestream is achieved by subtracting the freestream fluxes from the governing equations.

In the LU-ADI algorithm, each ADI operator is rewritten using the diagonal form[12,13] and the flux vector splitting technique.[14] For example, in the ξ direction,

$$I + h\delta_\xi \hat{A} = T_\xi \left(I + h\delta_\xi^b \hat{D}_A^+ + h\delta_\xi^f \hat{D}_A^- \right) T_\xi^{-1}$$

$$= T_\xi \left(I - \alpha h \hat{D}_{A_j}^- + h\delta_\xi^b \hat{D}_A^+ \right) \left(I + \alpha h |\hat{D}_{A_j}| \right)^{-1}$$

$$\times \left(I + \alpha h \hat{D}_{A_j}^+ h\delta_\xi^f \hat{D}_A^- \right) T_\xi^{-1} \quad (4)$$

where α is a coefficient appearing on the j index for the upwind differencing. In other words, $\alpha = 1.0$ when first-order differencing is used for the ξ derivative and 1.5 when second-order differencing is used. Currently, α is set to be 7/6, since three-point first-order differencing is used for the ξ derivative to be consistent with the fourth-order differencing in the right-hand side convective terms. The decomposition used in Eq. (4) can be called approximate LDU factorization or diagonally dominant factorization. This decomposition is more stable than simple LU factorization since the diagonal element always has $|\hat{D}_A|$.

In the solution process, an inversion in one direction consists of one scalar forward sweep and one scalar backward sweep. Thus, the LU-ADI algorithm requires little additional memory and is easily vectorized. It may be noteworthy that an operator in each direction can be considered to be a single iteration of a symmetric Gauss Seidel relaxation. The terms $\hat{D}_A^\pm$ are modified to include an implicit artificial dissipation term. Another modification is necessary in the ζ direction to evaluate implicit viscous terms.[6]

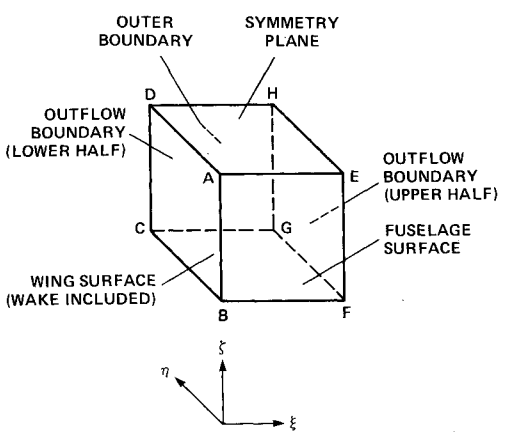

Fig. 2 Computational space corresponding to the physical space.

New Artificial Dissipation Model

The fourth-order dissipation model has been widely used with central differences in Navier-Stokes computations.[4,6,10] This constant-dissipation model reduces undesirable oscillations in the solution near discontinuities like shock waves. On the other hand, the second-order dissipation produced by proper upwinding works better than this fourth-order dissipation model in the region near the discontinuity. Such dissipation, however, is not desired for the rest of the flowfield, since it reduces the spatial accuracy to at most the first order. Higher-order TVD upwind schemes can be constructed by introducing antidiffusive terms, which should be accompanied by some form of limiters.

In the present study, a simplified model of such a limiter is considered. A numerical flux for the first-order upwind differencing of the convective terms can be written as

$$\hat{F}_{j+1/2} = \left(\hat{F}_j + \hat{F}_{j+1} \right)/2 - |\hat{A}_{j+1/2}| \left(\hat{Q}_{j+1} - \hat{Q}_j \right)/2 \quad (5)$$

Introducing a flux limiter ϕ to keep a global high-order accuracy, Eq. (5) is rewritten as

$$\hat{F}_{j+1/2} = \left(\hat{F}_j + \hat{F}_{j+1} \right)/2 - (I - \phi)|\hat{A}_{j+1/2}| \left(\hat{Q}_{j+1} - \hat{Q}_j \right)/2 \quad (6)$$

The matrix $|\hat{A}_{j+1/2}|$ is replaced by the spectral radius $\sigma = |U| + Cr_\xi$ so that the artificial dissipation terms are stable enough and can be simply evaluated. Equation (6), along with a proper evaluation of the limiter function (see Ref. 15, for instance), leads to a new artificial dissipation model which can be implemented in the central difference scheme. A fourth-order dissipation term is also necessary to maintain a global stability. The final form of the model is similar to that of an existing nonlinear model[13]:

$$h\nabla_\xi \left(\sigma J_{j+1/2} \right) \left[\left(I - \phi_{j+1/2} \right) \epsilon_2 \Delta_\xi J\hat{Q} - \phi_{j+1/2} \epsilon_4 \Delta_\xi \nabla_\xi \Delta_\xi J\hat{Q} \right] \quad (7)$$

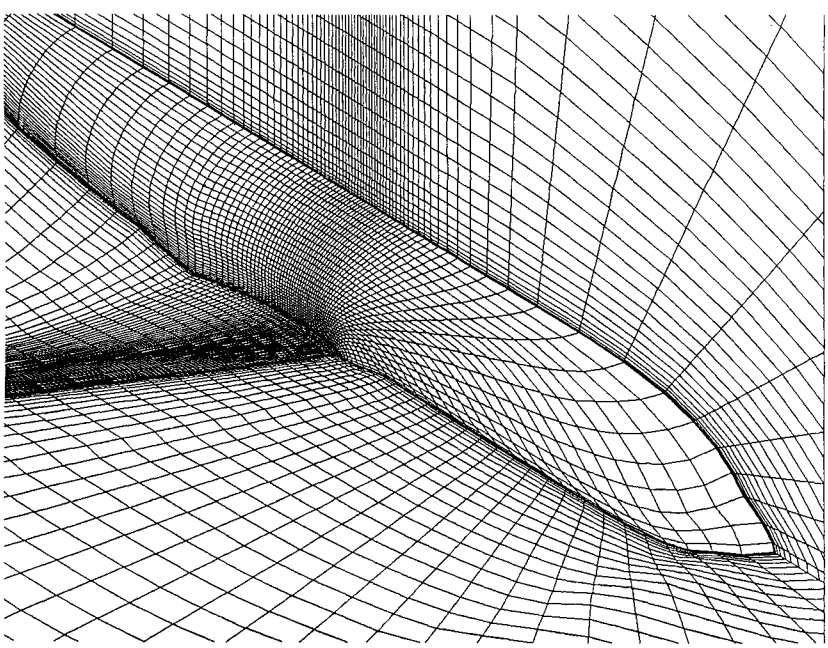

Fig. 3 Close-up view of the discretized region.

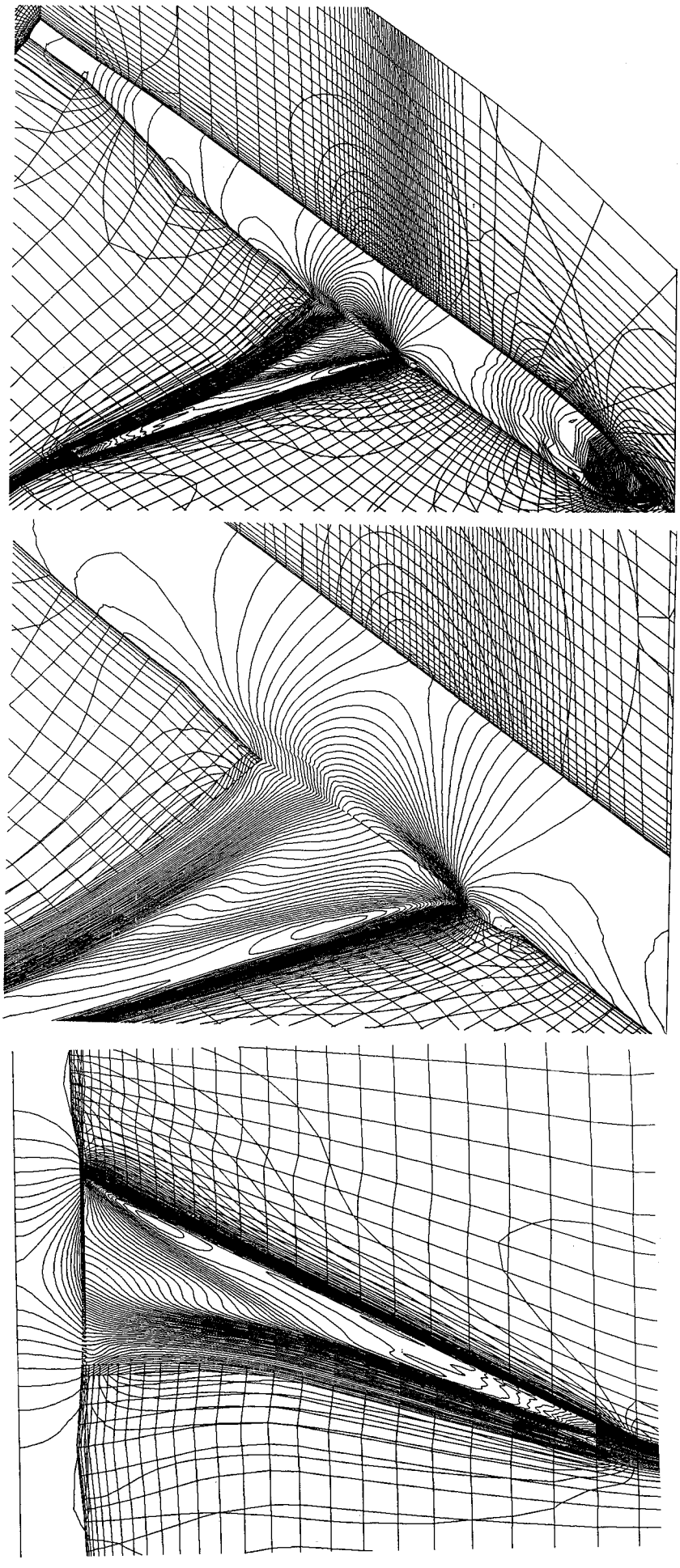

Fig. 4 Computed pressure contour plots ($M_\infty = 0.82$, $Re = 1.67 \times 10^6$, and $\alpha = 2.18$ deg): a) overall view, b) close-up view, and c) top view.

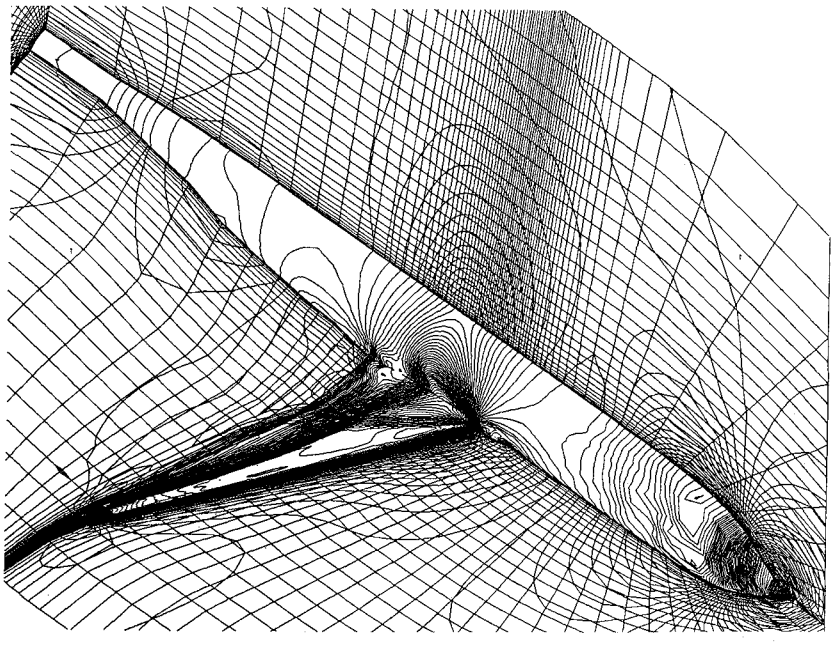

a)

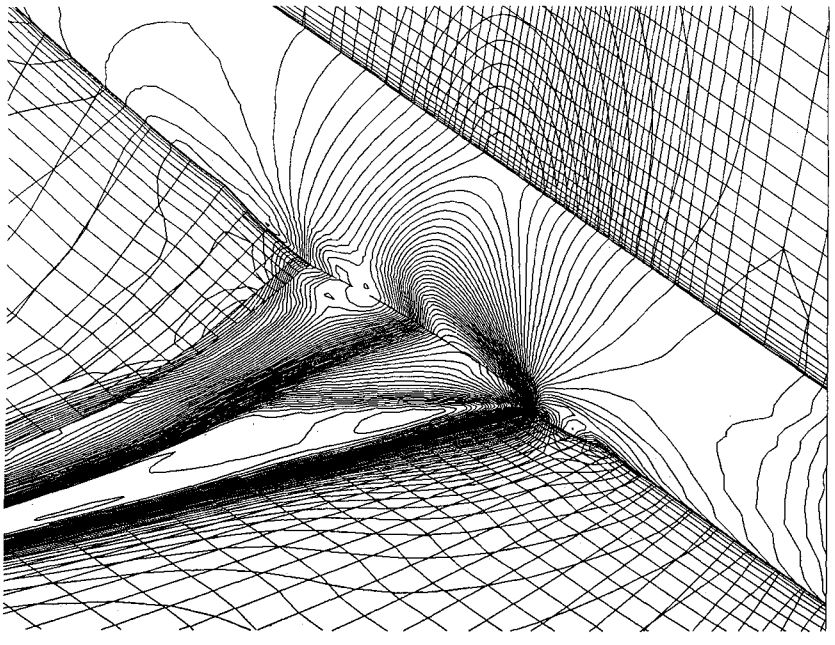

b)

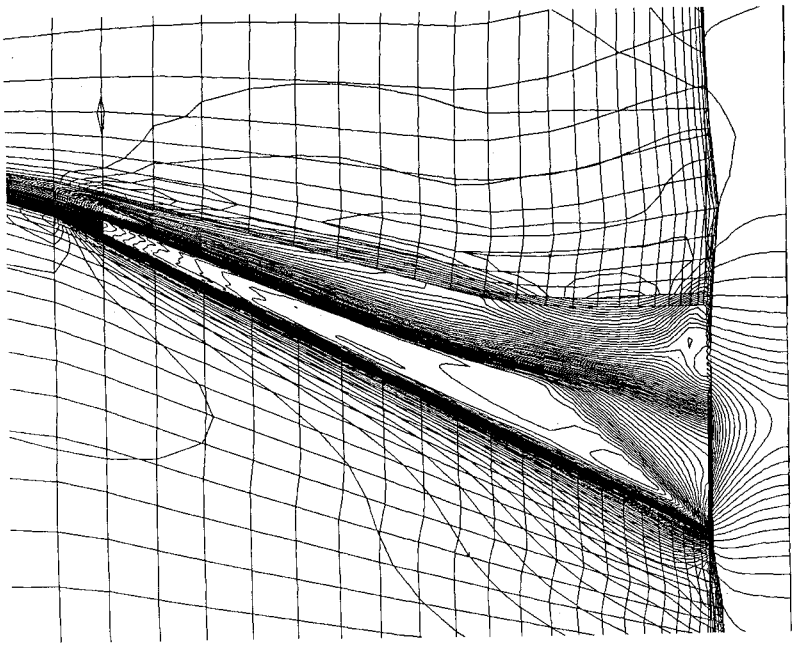

c)

Fig. 5 Computed pressure contour plots ($M_\infty = 0.82$, $Re = 1.67 \times 10^6$, and $\alpha = 4.00$ deg): a) overall view, b) close-up view, and c) top view.

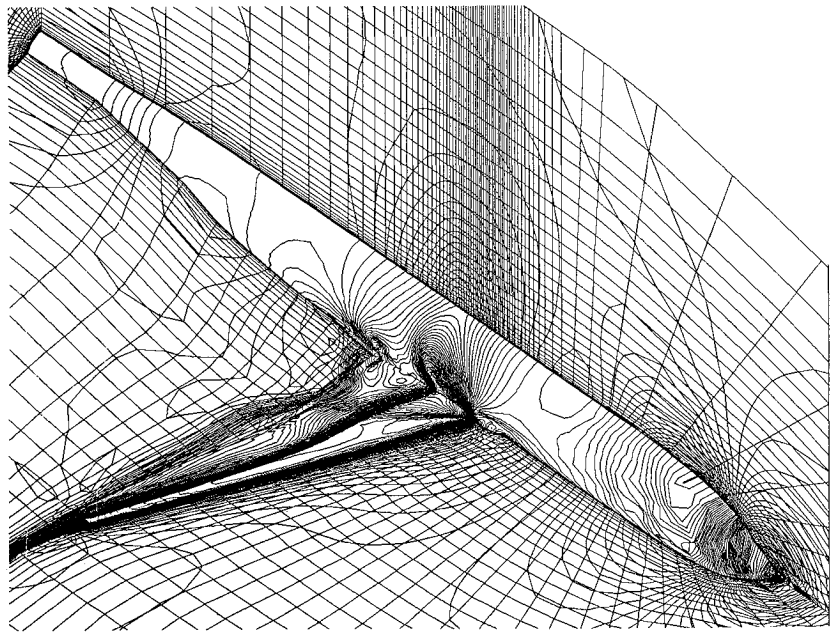

a)

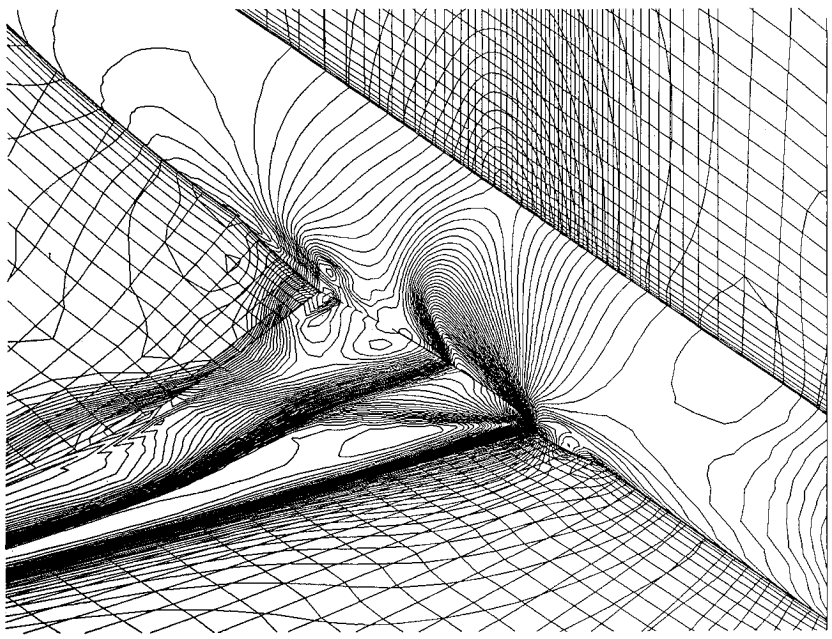

b)

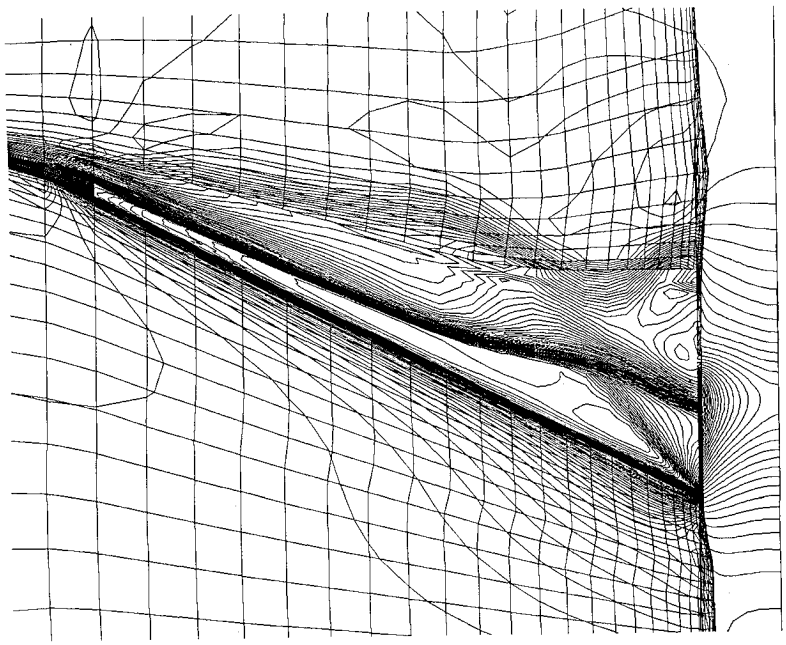

c)

Fig. 6 Computed pressure contour plots ($M_\infty = 0.82$, $Re = 1.67 \times 10^6$, and $\alpha = 6.00$ deg): a) overall view, b) close-up view, and c) top view.

where the suffix $j+1/2$ denotes the simple average of the j and $j+1$ indices. On the implicit side, only the fourth-order terms, corresponding to Eq. (7) with ϕ to be I, are included. This new dissipation model has been used for two-dimensional computations and has produced good results.[9]

Results

In order to demonstrate the developed code's applicability to practical problems, flow simulations about a wing-fuselage combination called "W-18," which was designed as a transonic transport aircraft, are carried out. The overall discretized region is shown in Fig. 1. Only the upper-half volume is plotted to show the grid clearly. Flow symmetry is assumed along the fuselage symmetry plane, and only the left-half volume is computed. The corresponding computational space is shown in Fig. 2. The grid topology is the C-H type. The fuselage surface corresponds to $K=1$, and the wing surface, including the wake cut, corresponds to $L=1$. Since there are boundary layers not only over the wing surface but also over the fuselage surface, the concentration of the grid at both surfaces is necessary. A close-up view near the root of the wing and the front of the fuselage is shown in Fig. 3. The grid contains 62 points in the η direction and 74 points in the ζ direction. In the ξ direction, 151 points are used to capture the canopy of the fuselage. Every second grid point in the η and ζ directions is depicted in all of these figures because of the limitations of the graphics. The canopy of the fuselage can be recognized, although the grid distribution is not fine enough to describe it because of the topological deficiency.

A freestream boundary condition is specified at the inflow and the outer boundary. The pressure is fixed to be the freestream value, and an extrapolation of the remaining physical variables is used at the outflow boundary. Flow symmetry is assumed at the bilateral symmetry plane. The freestream Mach number is fixed at 0.82 and the Reynolds number based on the root chord is 1.67×10^6, corresponding to the experiment. Computations are carried out for five angles of atack.

Figures 4a–4c show the computed pressure contours at a 2.18-deg angle of attack. Contours are plotted for several grid surfaces in the upper-half volume. Figure 4a is an overall view, Fig. 4b is a close-up view of the wing-fuselage junction, and Fig. 4c shows the view from the top. Compression waves in the spanwise direction are observed from the leading edge at the root section and create a clear shock wave by coalescing with compression waves from the rear portion. Figure 4c indicates that the pressure distribution is almost two-dimensional, even downstream of the shock wave.

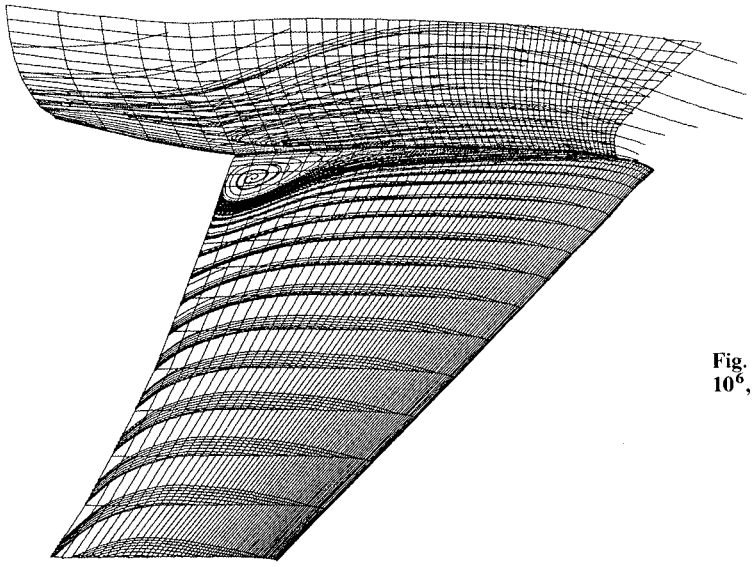

Fig. 7 Computed surface oilflow pattern ($M_\infty = 0.82$, $Re = 1.67\times10^6$, and $\alpha = 2.18$ deg).

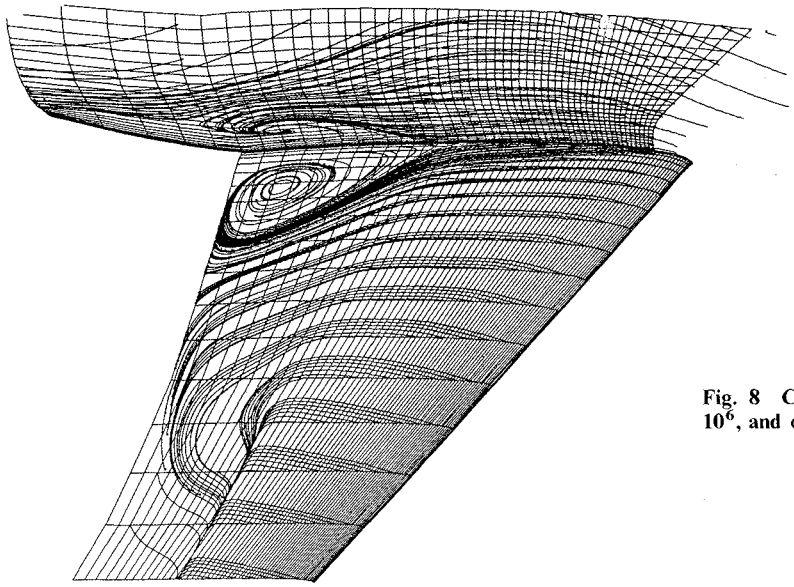

Fig. 8 Computed surface oilflow pattern ($M_\infty = 0.82$, $Re = 1.67\times10^6$, and $\alpha = 4.00$ deg).

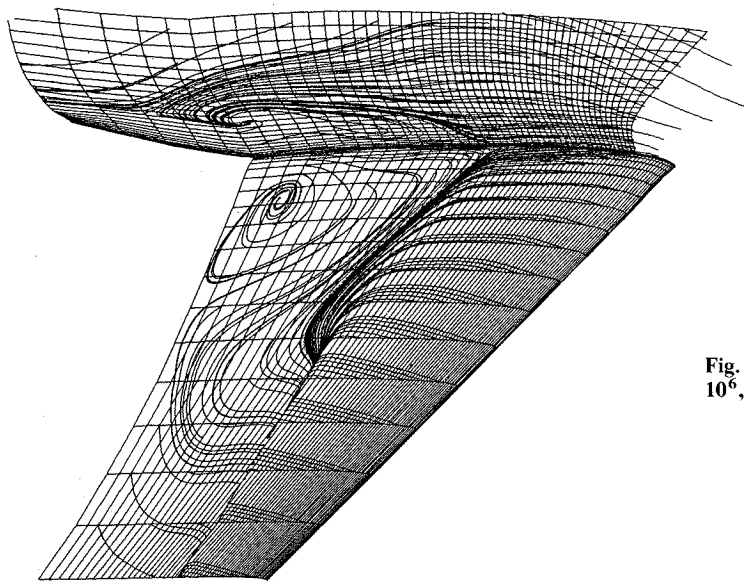

Fig. 9 Computed surface oilflow pattern ($M_\infty = 0.82$, $Re = 1.67 \times 10^6$, and $\alpha = 6.00$ deg).

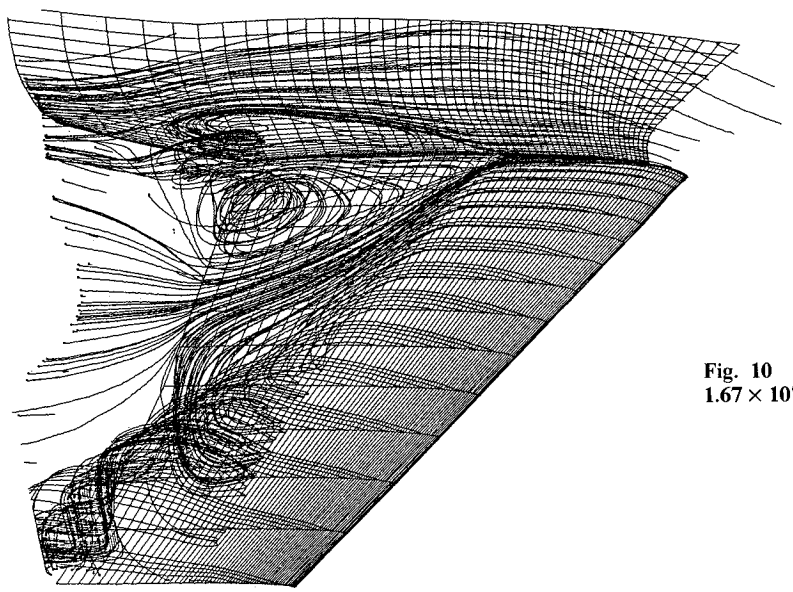

Fig. 10 Computed off-body particle path traces ($M_\infty = 0.82$, $Re = 1.67 \times 10^6$, and $\alpha = 6.00$ deg).

The computed result for the 4.0-deg angle-of-attack case is shown in Figs. 5a–5c in terms of the pressure contour plots. In Figs. 5b and 5c, shock-induced flow separation is recognized. Also, the shock wave is more pronounced and the junction of two compression waves from the root section is at the more inboard location.

The results for the 6.0-deg case are shown in Figs. 6a–6c. The shock-induced separation near the root section becomes larger, and the shock wave exists, even at the fuselage surface. The shock wave has a strong spanwise curvature and is located further upstream than the lower angle of attack cases. The wing surface pressure contours show that the flowfield after the shock wave is not two-dimensional as is the case for an isolated wing. For an isolated wing computation, the shock wave is always perpendicular to the symmetry plane (see Fig. 13 in Ref. 7, for instance). On the other hand, in Fig. 6c, the shock wave curves forward at the root section because of the wing-fuselage interaction. In other words, the fuselage has a large effect in the inboard region.

Computed surface oilflow patterns are shown in Figs. 7–9 for the three preceding cases. As is expected, the flowfield is quite gradual, and no shock-induced separation is seen in Fig. 7. At the junction of the fuselage and the wing, a small, flat recirculating region is observed near the trailing edge. In the other two cases, however, shock-induced separation is clearly seen. There also exists a large, three-dimensional separation near the junction because of the viscous effect over the fuselage, and the recirculating region becomes larger with an increasing angle of attack. To show the flow structure in this recirculating region, off-body particle traces are shown in Fig. 10 for a 6.0-deg angle of attack. The vortex in this region resembles a coiled spring which is bent 90 deg so that the vortex axis is perpendicular to both the wing and the fuselage surfaces. Further outboard on the wing, vortical flow toward the tip is seen. For a swept wing, this kind of spiral vortex is characteristic of the separated region induced by the shock wave.[7]

The comparison with the experiment at a 4.0-deg angle of attack is presented in Fig. 11 for the wing surface pressure distributions and in Fig. 12 for the fuselage surface pressure distributions. The overall agreement is fairly good, not only for the wing but also for the fuselage. The pressure at the trailing edge is well predicted, even for this postbuffet onset condition, which is important for aircraft design. It should be

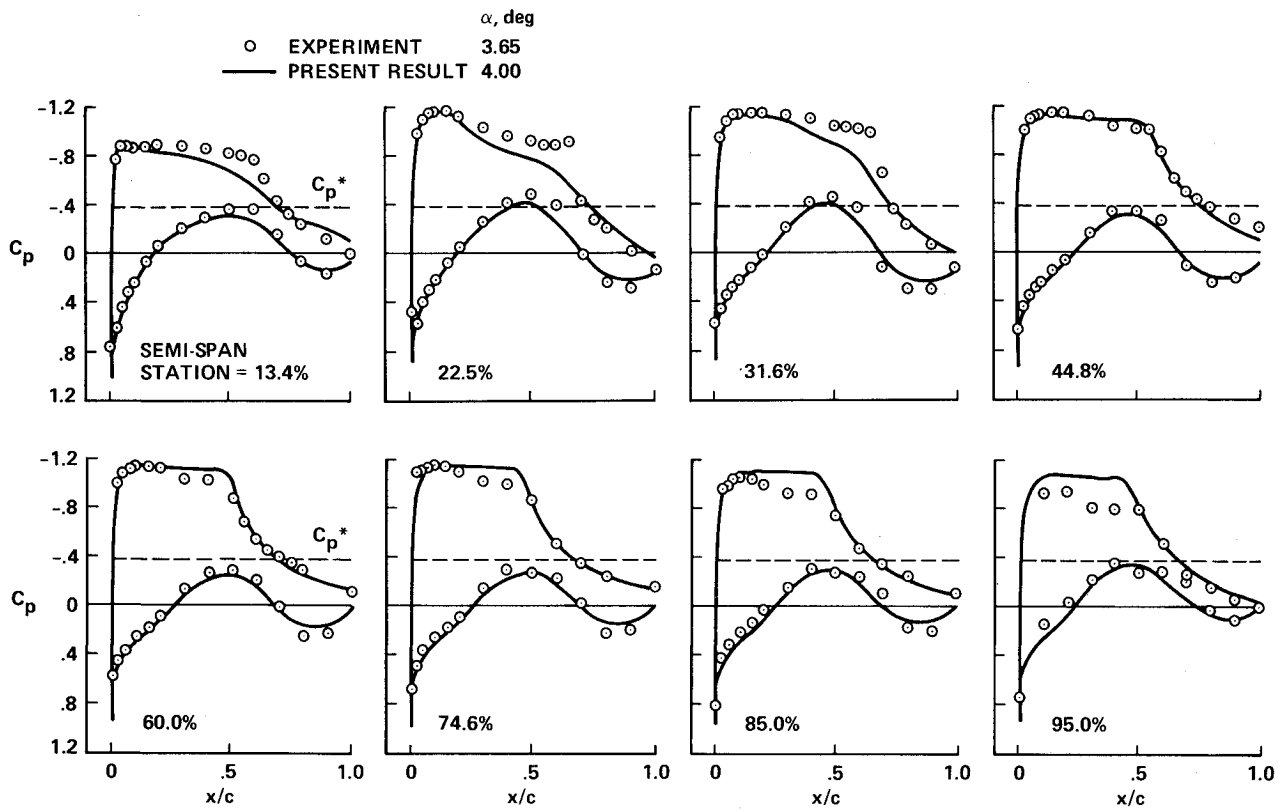

Fig. 11 Chordwise *Cp* distributions over a wing surface at several spanwise stations ($M_\infty = 0.82$, $Re = 1.67 \times 10^6$, and $\alpha = 4.00$ deg).

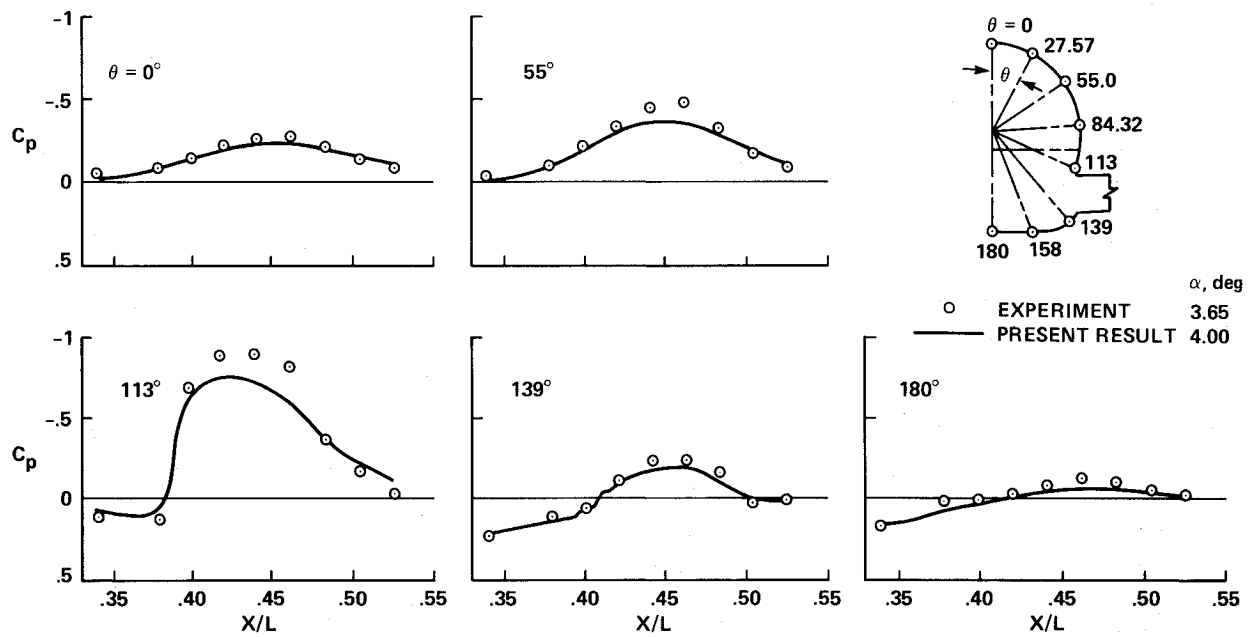

Fig. 12 Chordwise C_p distributions over a fuselage at several circumferential stations ($M_\infty = 0.82$, $Re = 1.67 \times 10^6$, and $\alpha = 4.00$ deg).

noted that the discrepancy in the pressure level at the tip section can be explained by the elastic deformation of the test model in the experiment. It is possible that the tip section of the steel model was twisted by aerodynamic forces, since the aspect ratio of the wing is very high. The detailed comparison with the experiment is described in Ref. 16.

The code is generally vectorized for supercomputers, and it required 9.5 μs per grid point per iteration on a Fujitsu VP 400 supercomputer. Compared to the computations over an isolated wing,[7] there was about a 40% CPU time increase, mainly because of the necessity to evaluate viscous terms and the eddy viscosity associated with them in one more direction. The other contributing factor is the new artificial dissipation, which requires more computing time than the simple fourth-order dissipation. In total, about 5–6 h were required to obtain the converged solution for each case.

Summary and Conclusions

Computations of transonic flows over a practical wing-fuselage geometry designed for a transonic transport aircraft

were carried out using three-dimensional Reynolds-averaged thin-layer Navier-Stokes equations. The thin-layer approximation is extended to two directions in order to evaluate viscous layers on the fuselage surface as well as the wing surface. The LU-ADI factorization algorithm was successfully used with the implementation of new smoothing terms. Computations were done for several angles of attack on the specified Mach and Reynolds numbers corresponding to the experiment. The comparison of the computed surface pressure with the experiment showed good agreement. The computed results revealed the effect of the fuselage near the wing root, especially at relatively high angles of attack. It was shown that the flow pattern when a fuselage exists is quite different from that for an isolated wing. This indicated the importance of the computation over a wing-fuselage combination using Navier-Stokes equations. The computation, which used about 700,000 grid points for each case, required about 5–6 h of computer time on a Japanese supercomputer.

Acknowledgment

The authors would like to express their gratitude to Japan Aircraft Development Corporation (JADC) and Mitsubishi Heavy Industry (MHI) for the wing geometry data and for their assistance. The authors would like to give special thanks to Mr. Susumu Shirayama, a Graduate Student of the University of Tokyo, for the development of the graphic programs used herein.

References

[1] Rubbert, P., "The Emergence of Advanced Computational Methods in the Aerodynamic Design of Commercial Transport Aircraft," International Symposium on Computational Fluid Dynamics-Tokyo, Tokyo, Sept. 1985.

[2] Holst, T.L., et al., AIAA Paper 85-1640, July 1985.

[3] Kordulla, W. and MacCormack, R.W., "A New Predictor-Corrector Scheme for the Simulation of Three-Dimensional Compressible Flows with Separation," AIAA Paper 85-1502, July 1985.

[4] Vadyak, J., "Simulation of Wing, Fuselage, and Wing/Fuselage Flowfield Using a Three-Dimensional Euler/Navier-Stokes Algorithm," AIAA Paper 85-1693, July 1985.

[5] Obayashi, S. and Kuwahara, K., "An Approximate LU Factorization Method for the Compressible Navier-Stokes Equations," *Journal of Computational Plysics*, Vol. 63, No. 1, March 1986, pp. 157–167.

[6] Obayashi, S. and Fujii, K., "Computation of Three-Dimensional Viscous Transonic Flows with the LU Factored Scheme," AIAA Paper 85-1510, July 1985.

[7] Fujii, K. and Obayashi, S., "Practical Application of New LU-ADI Scheme for the Three-Dimensional Navier-Stokes Computations of Transonic Flows," AIAA Paper 86-513, Jan. 1986.

[8] Fujii, K. and Obayashi, S., "Navier-Stokes Simulations of Transonic Flows over a Practical Wing Configuration," *AIAA Journal*, Vol. 25, March 1987, pp. 369–370.

[9] Obayashi, S., Matsushima, K., Fujii, K., and Kuwahara, K., "Improvements in Efficiency and Reliability for Navier-Stokes Computations Using the LU-ADI Factorization Algorithm," AIAA Paper 86-0338, Jan. 1986.

[10] Hung, C.-M. and Buning, P.G., "Simulation of Blunt-Fin Induced Shock Wave and Turbulent Boundary-Layer Interaction," *Journal of Fluid Mechanics*, Vol. 154, 1985, pp. 163–167.

[11] Pulliam, T.H. and Steger, J.L., "Implicit Finite Difference Simulations of Three-Dimensional Compressible Flow," *AIAA Journal*, Vol. 18, Feb. 1980, pp. 159–167.

[12] Pulliam, T.H. and Chaussee, D.S., "A Diagonal Form of an Implicit Approximate Factorization Algorithm," *Journal of Computational Physics*, Vol. 39, 1981, pp. 347–363.

[13] Pulliam, T.H. and Steger, J.L., "Recent Improvement in Efficiency, Accuracy, and Convergence for Implicit Approximate Factorization Algorithms, AIAA Paper 85-360, Jan. 1985.

[14] Steger, J.L. and Warming, R.F., "Flux Vector Splitting of the Inviscid Gasdynamic Equations with Application to Finite-Difference Methods," *Journal of Computational Physics*, Vol. 40, 1981, pp. 263–293.

[15] Sweby, P.K., "High Resolution Schemes Using Flux Limiters for Hyperbolic Conservation Laws," *SIAM Journal of Numerical Analysis*, Vol. 21, No. 4, 1984, pp. 995–1011.

[16] Miyakawa, J., Jakanashi, S., Fujii, K., and Amano, K., "Searching the Horizon of Navier-Stokes Simulation of Transonic Aircraft," AIAA Paper 87-0524, Jan. 1987.